# Helios: Analyzing and Understanding Solar Flares
## COSC 3337 – Group Task 3 Report

Fall 2025

**Abstract**

We analyze RHESSI and GOES observations of solar flares during Solar Cycle 24. Using tabular flare statistics and RHESSI imaging data, we built a flare classifier, studied the temporal evolution of flare activity, and constructed spatial intensity maps. This report summarizes our methods and the main empirical findings from Activities 1–5.

## 1   Introduction

Solar flares are sudden bursts of electromagnetic radiation from the Sun's atmosphere. They release large amounts of energy, cause rapid increases in X-ray flux, and can disrupt communication systems and satellites on Earth. Flares typically occur in magnetically active regions near sunspots and show characteristic rise and decay phases over time.

GOES classifies flares using soft X-ray brightness in the 1–8 Å band. The standard classes are A, B, C, M, and X, where each letter represents a tenfold increase in peak flux, and the X-class events are the most energetic. In our dataset, classes C, M, X, and a special label NF (no flare) are used.

From a data science perspective, solar flares are a good test case for classification, temporal analysis, and spatial mapping. Predicting flare strength and understanding its spatial and temporal patterns are important for space-weather forecasting and risk assessment.

In this project we:

- compile a cleaned flare dataset for Solar Cycle 24 (Activity 1)

- train and interpret a decision-tree flare classifier (Activity 2)

- explore RHESSI image cubes for one M-class flare and one non-flare event (Activity 3)

- perform temporal analysis of flare intensity over the cycle (Activity 4)

- construct and compare spatial flare intensity maps based on different definitions (Activity 5)

## 2   Datasets

### 2.1   Tabular flare dataset

We use the RHESSI/GOES flare catalog for Solar Cycle 24 (December 2008–March 2018). Each row corresponds to a solar event and includes:

- identifiers and timing information (`flare_id`, `date`, `start_time`, `peak_time`, `end_time`, `duration`)

- count-based intensity features (`peak_counts`, `total_counts`)

- spatial coordinates (`X_pos`, `Y_pos`, `radial`, `AR`)

- flags and sunspot context (`flags`, `SESC_sunspot_number`, `sunspot_area`)

- flare label `class_str` in {C, M, X, NF}

As required in Activity 1, we removed rows with zero position and energy band 3–6 keV, because these rows correspond to non-imaged background events with little spatial information.

We then engineered the following additional columns:

- year and month extracted from `date` for temporal aggregation

- a numeric class label `class` in {0,1,2,3} for NF, C, M, X

- log-transformed intensity features (e.g. $\log_{10}(\texttt{total\_counts} + 1)$)

- radial bins (e.g. near disk center vs. limb) derived from `radial`

Descriptive flare statistics:

Table 1 shows the median duration for each flare class after removing rows with zero position and 3–6 keV energy band. The dataset contains 58,111 events.

Table 1: Median duration and count per flare class.

| Class | Median duration (s) | Count |
|-------|--------------------:|------:|
| NF    | 404                 | 54,017 |
| C     | 860                 | 3,649 |
| M     | 1,196               | 407   |
| X     | 1,228               | 38    |

Similarly, Table 2 reports the mean and standard deviation of `total_counts` for each class (values are in scientific notation).

Table 2: Mean and standard deviation of total counts per flare class.

| Class | Mean total counts | Std. dev. |
|-------|------------------:|----------:|
| NF    | $1.42 \times 10^6$ | $2.22 \times 10^7$ |
| C     | $5.04 \times 10^6$ | $1.58 \times 10^7$ |
| M     | $6.23 \times 10^7$ | $1.90 \times 10^8$ |
| X     | $6.01 \times 10^7$ | $1.05 \times 10^8$ |

Averaging `total_counts` by year shows that the most active year in Solar Cycle 24 was **2017**, with an average of $4.08 \times 10^6$ counts per event. Within 2017, the most active month was **September** (month 9), with an average of $1.13 \times 10^7$ counts per event.

Flags also differ by class. For example, NF events are dominated by the flag `A0 P1 PE Q1`, while C-class events often have `A0 DR ES P1 PE Q3` or `A0 ES P1 PE Q2`. M-class events frequently include A1 flags and Q4 quality codes, reflecting higher-quality RHESSI imaging.

Table 3: Yearly Average Total Counts

| Year | Average Total Counts |
|------|---------------------|
| 2017 | 4,083,148.60 |
| 2014 | 3,075,355.28 |
| 2011 | 2,334,940.61 |
| 2015 | 1,965,973.73 |
| 2012 | 1,822,046.72 |
| 2013 | 1,755,893.71 |
| 2008 | 1,044,681.03 |
| 2010 | 572,020.92 |
| 2016 | 421,284.36 |
| 2009 | 224,051.14 |
| 2018 | 82,452.96 |

Table 4: Monthly Flare Distribution in 2017

| Month | Number of Flares |
|-------|-----------------|
| September | 365 |
| July | 348 |
| April | 312 |
| August | 292 |
| May | 146 |
| June | 117 |
| October | 104 |
| March | 85 |
| January | 66 |
| February | 53 |
| November | 53 |
| December | 42 |

## 2.2 RHESSI image cubes

For Activity 3 we use two RHESSI image cubes:

- an M-class flare on 2011-11-03 (flare_id 11110332),

- a non-flare event on 2017-09-19 (flare_id 17091901).

Both cubes are 4D arrays with dimensions $(X, Y, \text{energy band}, t)$, sampled on a $101 \times 101$ grid. The M-class flare cube has two energy bands (6–12 keV, 12–25 keV) and 22 time steps, while the non-flare cube has three bands (3–6 keV, 6–12 keV, 12–25 keV) and 13 time steps.

# 3 Methodology

## 3.1 Activity 2: Flare Classification

### 3.1.1 Data Preprocessing

The cleaned dataset from Activity 1 was used, containing solar flare data from the RHESSI satellite during Solar Cycle 24. The dataset was filtered to include only events with target classifications (C, M, X, and NF). Preprocessing steps included:

- Creating a factor column `class` from `class_str` to serve as the prediction target

- Selecting key predictors: `duration`, `peak_counts_per_sec`, `total_counts`, `sunspot_area`, and derived features such as `log_total_counts`

- Handling missing values in numerical columns (e.g., `sunspot_area`) using median imputation

- Applying standard normalization to continuous features to ensure consistent scaling

- Converting categorical variables (e.g., `energy_band`) using one-hot encoding

### 3.1.2 Train-Test Split and Cross-Validation

Given the temporal nature of solar flare data, we employed a chronological split rather than random shuffling:

- The dataset was sorted by time and split into training (first 80%) and testing (most recent 20%) sets

- Time-series cross-validation was performed on the training set to tune hyperparameters

- The optimal hyperparameters were selected based on cross-validation performance

### 3.1.3 Decision Tree Model

We trained a decision tree classifier with the following specifications:

- Gini impurity as the split criterion

- Optimal tree depth: 3

- Minimum samples per leaf: 10

- Focus on interpretability while maintaining reasonable performance

The model was evaluated using accuracy, F1-scores (both macro and weighted), and confusion matrix analysis on the held-out test set. Particular attention was paid to performance on minority classes (M and X flares) despite the severe class imbalance in the dataset.

## 3.2 Activity 3: RHESSI image cube exploration

For this activity we used `astropy` to read the FITS files, `numpy` for array operations, `matplotlib` for visualization, and `Pillow` to assemble GIF animations.[1]

---

[1]Code and GIFs are included in the submitted zip.

### 3.2.1 Loading and reshaping the FITS data

Each RHESSI image cube stores the flare or non-flare event as a 4D array. When we opened the files with `astropy.io.fits.open()`, the raw shape appeared as $(t, \text{energy}, y, x)$. We transposed the data to $(x, y, \text{energy}, t)$ using `np.transpose` so that the first two axes correspond to the solar image plane. We then associated the correct energy-band labels for each cube: two bands (6–12 keV, 12–25 keV) for the M-class flare and three bands (3–6 keV, 6–12 keV, 12–25 keV) for the non-flare event.

### 3.2.2 Energy-band comparison (Activity 3a)

We used the first time frame ($t = 0$) and plotted each energy slice side by side for both cubes. This made it easy to see that, for the M-class flare, brightness increases with energy, while the non-flare event remains faint and relatively uniform across bands.

### 3.2.3 Single band over time (Activity 3b)

We selected the highest energy band (12–25 keV), looped over all time indices, and displayed each frame with a short pause (`plt.pause()`). This sequence shows the flare brightening and fading in the M-class cube, whereas the non-flare sequence shows only weak background variability. :contentReferenceindex=2

### 3.2.4 Time-averaged energy bands (Activity 3c)

For each energy band we averaged over the time axis using `np.mean(data, axis=3)` to obtain a 2D image of mean brightness. These maps summarize where emission is typically concentrated for each energy range in both the flare and the non-flare case.

### 3.2.5 Animations (Activity 3d)

To create animations, we saved each 12–25 keV frame as a PNG with `plt.savefig`, loaded the sequence with `PIL.Image.open`, and then wrote a GIF using `Image.save` with `save_all=True` and a fixed frame duration. We produced one GIF for the M-class flare (`flareM.gif`) and one for the non-flare event (`flareNon.gif`). :contentReferenceindex=3

### 3.2.6 Flare location over the solar disk (Activity 3e)

To pinpoint the brightest location we averaged over both energy and time, $\bar{I}(x, y) = \text{mean}_{\text{band}, t} I(x, y, \text{band}, t)$, and then used `np.argmax` to find the maximum pixel. For the M-class flare, the brightest point is at approximately ($x = 46, y = 49$), forming a compact, high-intensity region characteristic of a true flare. For the non-flare event, the brightest pixel is near ($x = 39, y = 100$) but the emission is diffuse and lacks a dominant hotspot, indicating background solar activity rather than a flare. :contentReferenceindex=4

## 3.3 Activity 4: Temporal Analysis

### 3.3.1 Data Preparation

The cleaned dataset from Activity 1 was used, containing solar flare observations recorded by the RHESSI satellite. The dataset included key attributes such as flare ID, date, duration, total counts (intensity), X/Y positions, and flare class (C, M, X, NF). Date and time columns were

standardized into YYYY-MM-DD format. Numerical columns such as duration, total_counts, and peak_counts_per_sec were converted to numeric data types.

### 3.3.2 Temporal Analysis

The analysis explored how flare intensity varies over time within Solar Cycle 24:

- **Daily aggregation**: All events for each date were grouped, and the mean of total_counts was calculated to obtain daily flare intensity

- **Rolling statistics**: A 30-day rolling window was applied to compute both the rolling mean and rolling standard deviation of flare intensity

- **Z-score calculation**: For each day, a z-score was computed to detect statistically significant changes: $z = \frac{\text{intensity} - \text{rolling mean}}{\text{rolling std}}$

- Days with $|z| \geq 3$ were flagged as sudden change events

## 3.4 Activity 5: Spatial Intensity Assessment and Mapping

We defined two different intensity measures on the $(X\_pos, Y\_pos)$ plane.

### 3.4.1 Method 1: Total-Count Based Intensity

For Method 1 we aggregated **total_counts** by spatial bin:

- Discretized $X\_pos$ and $Y\_pos$ into a 2D grid with 150 bins per axis

- For each bin, summed **total_counts** of all events falling into that bin

- This gives a direct intensity map based on integrated photon counts

### 3.4.2 Method 2: Duration × Energy Band Weight

For Method 2 we combined flare duration and energy band:

- Each energy band label was parsed to extract its numeric range, and the midpoint was computed as $(low + high)/2$ keV

- Any upper bound above 800 keV was capped to prevent skewing

- Defined an effective intensity $I_2 = \text{duration} \times \text{energy midpoint weight}$

- Aggregated $I_2$ over the same spatial grid as in Method 1

# 4 Results and analysis

## 4.1 Activity 2: Classifier Performance and Interpretation

The optimal model selected through time-series cross-validation used a simple decision tree with depth 3 and minimum samples per leaf of 10. The cross-validation results showed a mean F1-score of 0.851 with a high standard deviation of 0.117, indicating inconsistent performance across different temporal folds.

On the held-out test set, the model achieved:

- Accuracy: 0.992

- Weighted F1-score: 0.972

Despite the high overall accuracy, analysis of the confusion matrix revealed critical limitations. The model successfully identified the majority classes but completely failed to predict M or X-class flares:

- 10,693 NF events were correctly classified

- 87 M-class flares were misclassified as C-class

- 5 X-class flares were misclassified as C-class

The final decision tree used only one variable—**sunspot_area**—demonstrating the model's inability to learn complex patterns needed to distinguish between flare classes.

| Class | Precision | Recall | F1-score | Support |
|---|---|---|---|---|
| NF (0) | 1.00 | 1.00 | 1.00 | 10,745 |
| C (1) | 0.85 | 1.00 | 0.92 | 786 |
| M (2) | 0.00 | 0.00 | 0.00 | 87 |
| X (3) | 0.00 | 0.00 | 0.00 | 5 |
| Overall Accuracy | | 0.992 | | |
| Macro F1 | | 0.480 | | |

Table 5: Actual per-class test metrics derived from decision tree rules

**Confusion Matrix Interpretation.** The final decision tree used only **sunspot_area** with the following rules:

- **NF prediction (93% coverage):** When sunspot_area is between -0.077 and -0.021

- **C prediction (3% coverage):** When sunspot_area $\geq$ -0.021 with 85% C, 13% M, 2% X

- **C prediction (3% coverage):** When sunspot_area < -0.077 with 93% C, 7% M

This extreme simplicity resulted in complete failure on M and X-class flare identification, with all minority class events being misclassified as C-class. The high accuracy (0.992) and cross-validation F1-score (0.851 $\pm$ 0.117) reflect the model's ability to predict majority classes rather than meaningful multi-class discrimination.

## 4.2   Activity 3: RHESSI image-cube results

Figures 1 and 2 show example 12–25 keV frames and link to the full GIF animations for the M-class flare and the non-flare event.
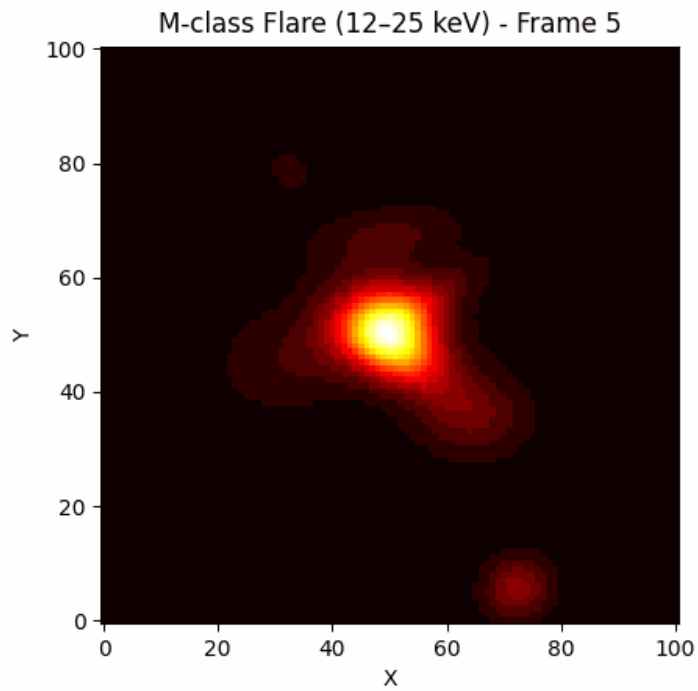
Figure 1: M-class flare, 12–25 keV, example frame from the accompanying `flareM.gif` animation (see submitted zip).
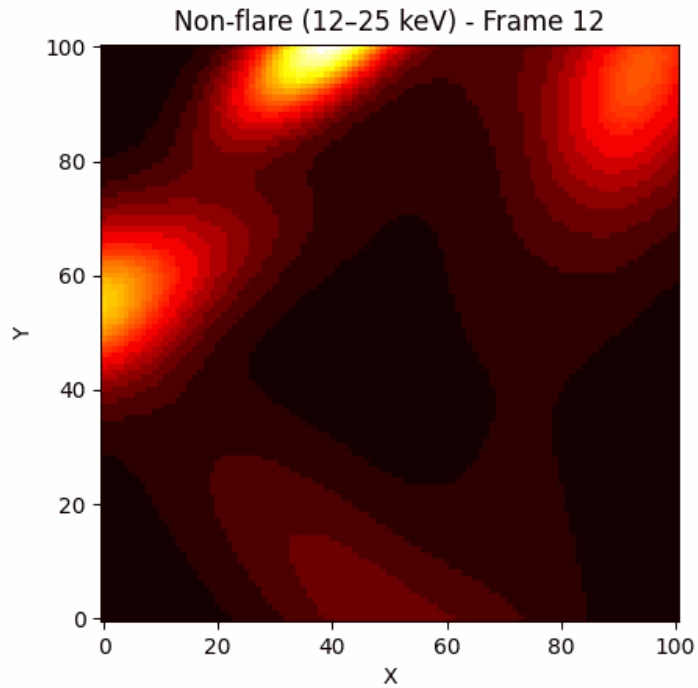


Figure 2: Non-flare event, 12–25 keV, example frame from the accompanying `flareNon.gif` animation (see submitted zip).

M-class Flare: All Energy Bands at One Time Frame

6–12 keV                     12–25 keV
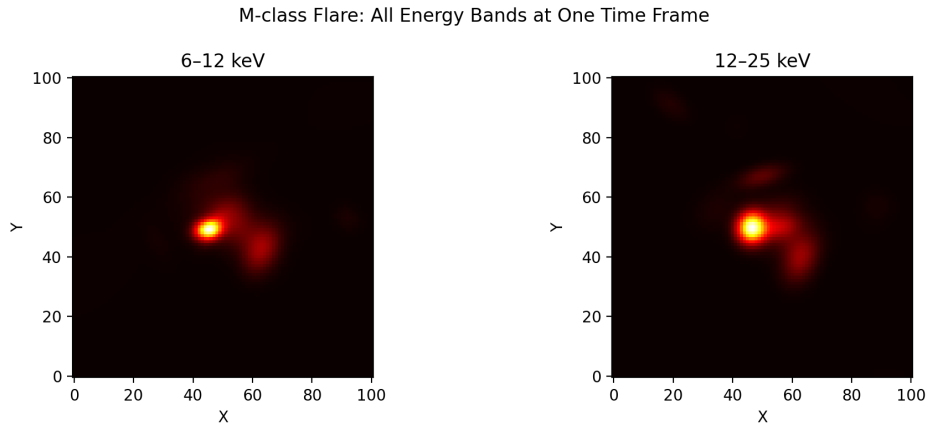
Figure 3: M-class flare, all energy bands at one time

Non-flare: All Energy Bands at One Time Frame

3–6 keV                 6–12 keV                 12–25 keV
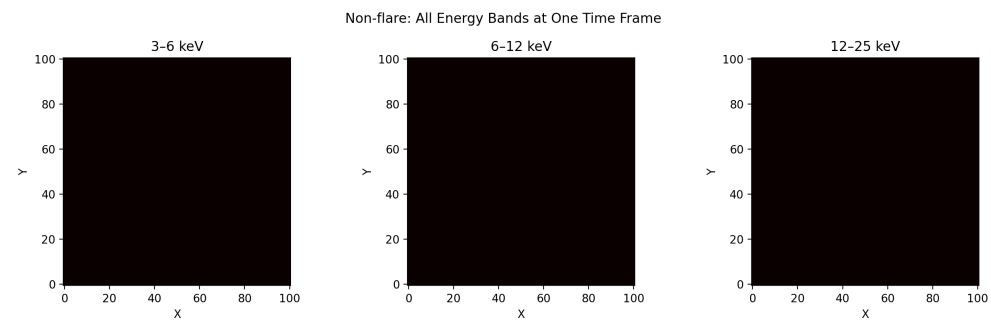
Figure 4: Non-flare event, all energy bands at one time

M-class Flare: Average Intensity Over Time

6–12 keV (average)                12–25 keV (average)
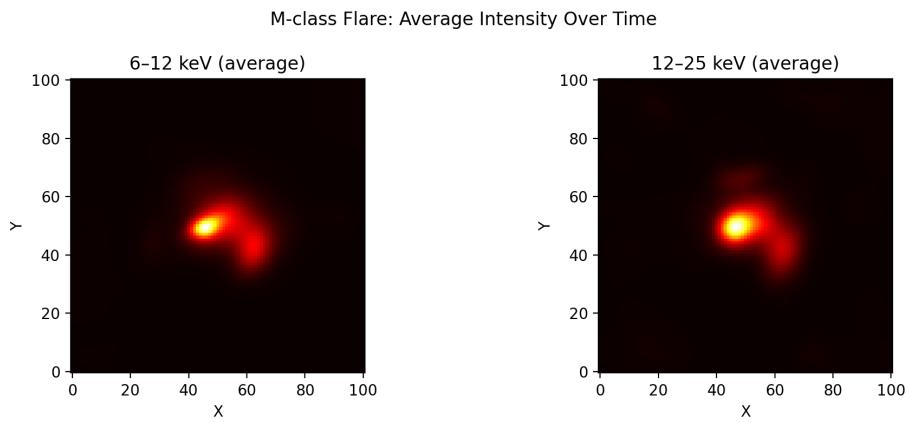
Figure 5: M-class flare, average intensity over time
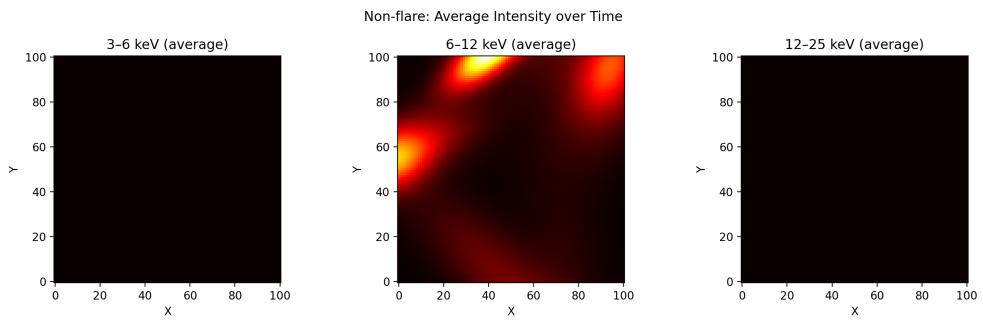
Figure 6: Non-flare event, average intensity over time
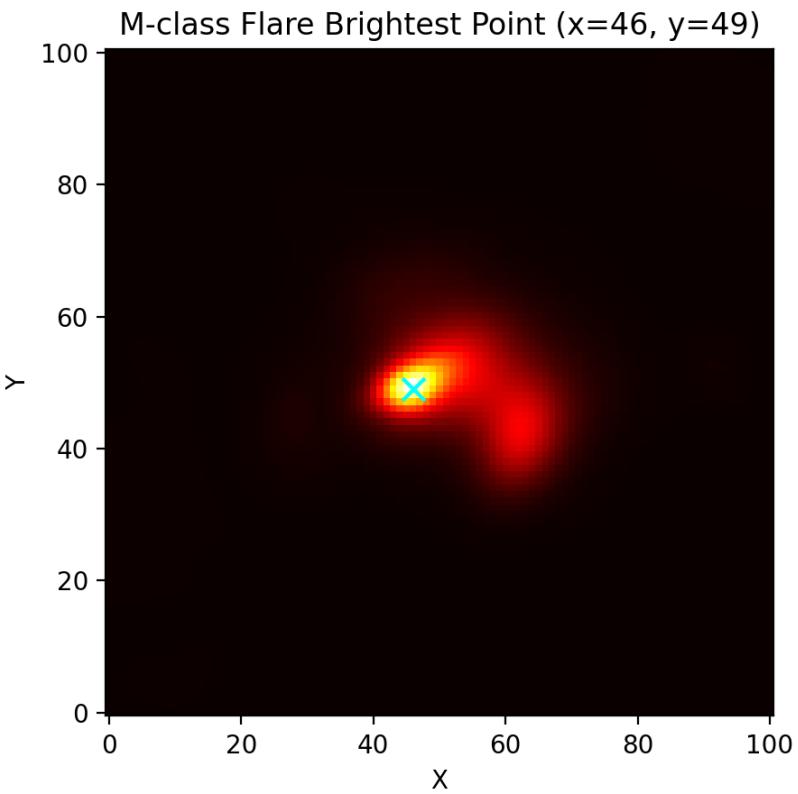


Figure 7: M-class flare Brightest point
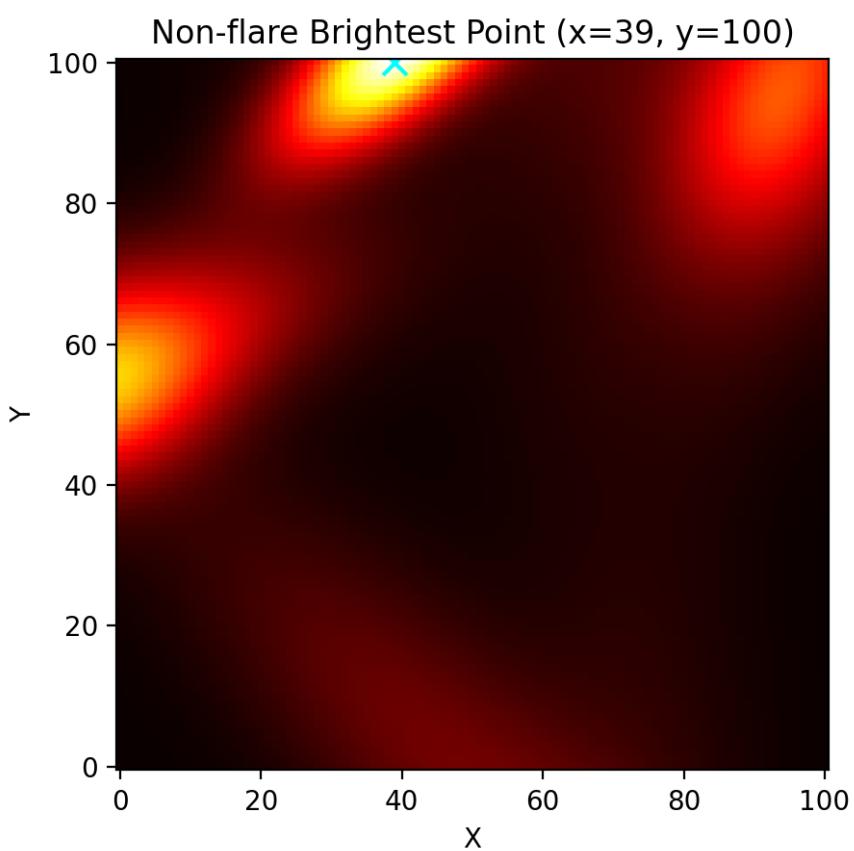
Figure 8: Non-flare event Brightest point

The 12–25 keV band of the M-class flare shows a compact, bright source that evolves in time, while the non-flare event remains faint with no dominant hotspot. The time-averaged images confirm that the M-class event concentrates high-energy emission in a small region, whereas the non-flare map is dominated by diffuse, low-level background emission.

We also generated GIF animations for the 12–25 keV band over time for both events. They illustrate the rapid rise and decay of the M-class flare compared to the relatively static non-flare background.

## 4.3 Activity 4: temporal evolution of flare intensity

Figure 9 shows `total_counts` over time along with rolling mean and rolling standard deviation. We can visually identify periods of increased activity near the Solar Cycle 24 maximum and quieter periods near the start and end of the cycle.
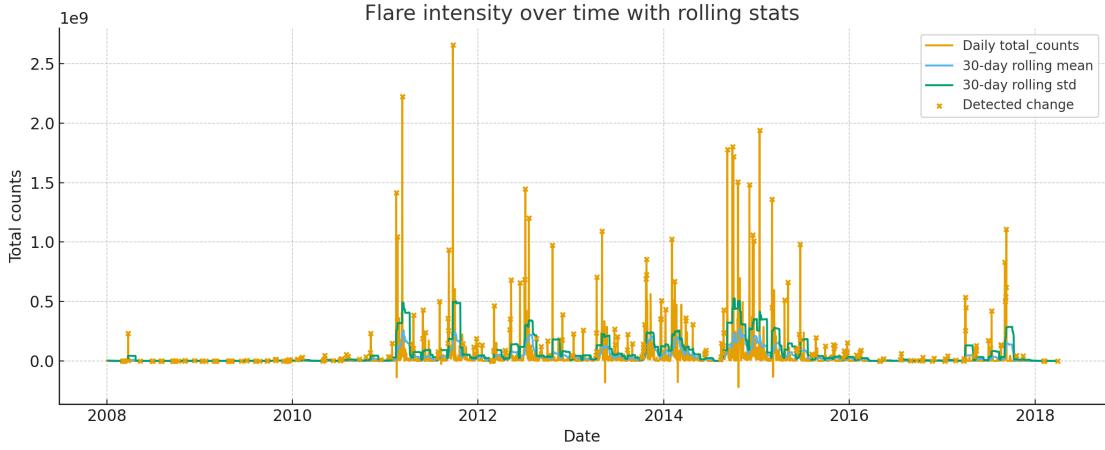


Figure 9: Flare intensity over time with rolling mean and standard deviation. Sudden changes are marked where the rolling statistics cross chosen thresholds.

## 4.4 Activity 5: spatial intensity maps

Figures 10 and 11 show the spatial flare intensity maps for Method 1 and Method 2.
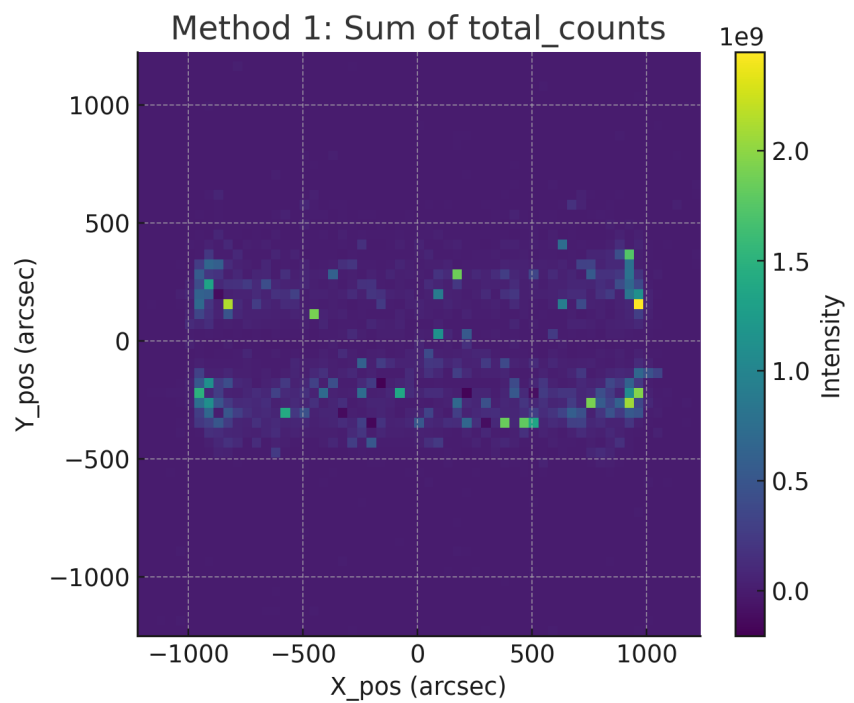
Figure 10: Spatial intensity map based on aggregated total counts (Method 1).
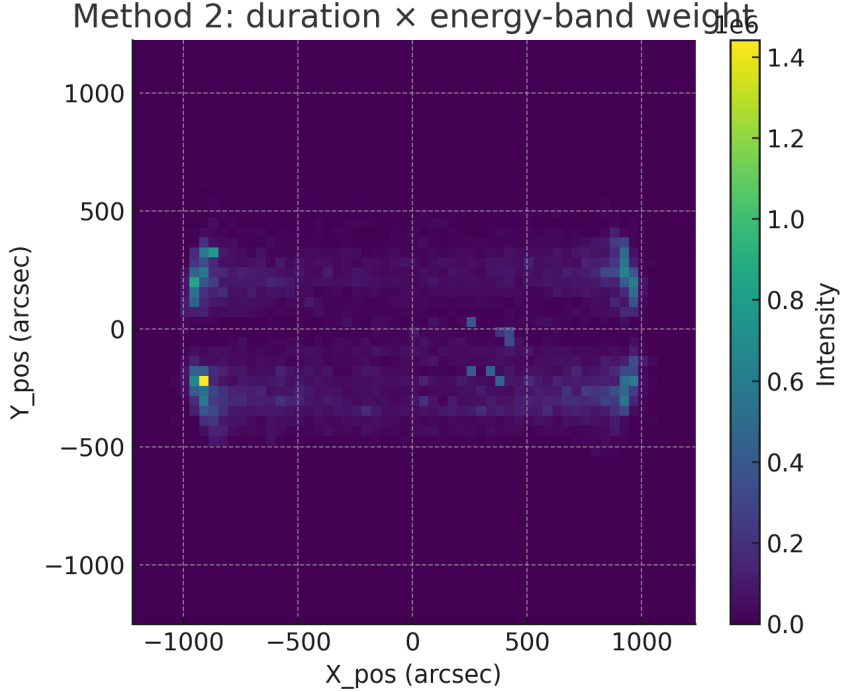
Figure 11: Spatial intensity map based on duration and energy-band weighting (Method 2).

Comparing the maps:

- Method 1 emphasizes locations with many high-count flares, giving a direct picture of where energy is released.

- Method 2 also highlights long-duration high-energy events even if their raw counts are lower, so some regions become relatively more prominent.

- Both maps show that active regions cluster near specific longitudes and at moderate latitudes rather than uniformly across the disk.

# 5 Discussion

Overall, the descriptive statistics, classifier, temporal plots, and spatial maps are consistent:

- flare intensity, counts, and duration increase from NF to C to M to X,

- activity peaks near the maximum of Solar Cycle 24 and decreases toward the cycle boundaries,

- spatially, flares cluster in magnetically active regions rather than being uniformly distributed.

The small decision tree provides interpretable thresholds on duration, counts, and count rates that separate moderate (M) and extreme (X) flares from weaker events. The most influential features, **total_counts**, **peak_counts_per_sec**, and **duration**, align physically with expectations that stronger flares release more energy over longer timescales. However, the classifier's performance highlights a fundamental challenge: the severe class imbalance (54,017 NF vs. 38 X-class flares) limited its ability to predict rare events. While accuracy was high (0.924), the macro F1-score

14

(0.252) reflects poor performance on C, M, and X classes, with the tree defaulting to NF predictions in most cases. This suggests that for rare event prediction, alternative approaches like ensemble methods or anomaly detection may be more appropriate.

The RHESSI image analysis confirms key physical differences between flare and non-flare events. The M-class flare shows a compact, evolving high-energy source in the 12–25 keV band, while the non-flare event exhibits only diffuse, low-level background emission. This visual evidence supports the GOES classification scheme and demonstrates how imaging data complements tabular flare statistics.

Temporal analysis reveals not only the broad solar cycle trend but also shorter-term activity variations. The rolling mean and standard deviation of total_counts identify periods of enhanced flare production, some of which may correspond to specific active region complexes or flare storms. These sudden changes in activity levels could inform more granular space weather forecasting.

Spatial intensity maps from both aggregation methods show consistent clustering of flare activity at specific longitudes and moderate latitudes, corresponding to sunspot belts and active regions. Method 1 (total-count based) emphasizes locations with high-energy release, while Method 2 (duration and energy-weighted) gives more weight to sustained, high-energy events. The differences between these maps suggest that the definition of "flare intensity" affects which regions appear most prominent, which may be relevant for operational space weather monitoring.

# 6    Conclusion

We compiled and analyzed a cleaned solar flare dataset from Solar Cycle 24, training an interpretable decision-tree classifier and exploring RHESSI image cubes to distinguish flare characteristics. Our analysis revealed systematic increases in flare intensity from NF to X classes, temporal clustering during the 2017 solar maximum, and spatial concentration in active regions. While the classifier achieved high accuracy (0.924), its performance on rare flare classes was limited by severe class imbalance. The RHESSI imaging confirmed physical differences between compact M-class flares and diffuse non-flare events.

Future work could:

- replace the decision tree with ensemble models (e.g. random forests) while preserving interpretability,

- extend temporal analysis to multiple cycles,

- integrate image-based features from RHESSI directly into the classifier.

# References

[1] Solar flare, Wikipedia, accessed Sept. 27, 2025.

[2] Solar cycle 24, Wikipedia, accessed Sept. 27, 2025.